Nano Scale Disruptive Silicon-Plasmonic Platform for Chip-to-Chip Interconnection

D5.3 optical filters (2nm bandwidth, >30nm FSR) and first generation beam shapers

Deliverable no.:	D5.3
Due date:	01/07/2013
Actual Submission date:	15/2/2014
Authors:	imec
Work package(s):	WP4
Distribution level:	RE[1] (NAVOLCHI Consortium)
Nature:	document, available online in the restricted area of the NAVOLCHI webpage

List of Partners concerned

Partner number	Partner name	Partner short name	Country	Date enter project	Date exit project
1	Karlsruher Institut für Technologie	KIT	Germany	M1	M36
2	INTERUNIVERSITAIR MICRO-ELECTRONICA CENTRUM VZW	IMEC	Belgium	M1	M36
3	TECHNISCHE UNIVERSITEIT EINDHOVEN	TU/e	Netherlands	M1	M36
4	RESEARCH AND EDUCATION LABORATORY IN INFORMATION TECHNOLOGIES	AIT	Greece	M1	M36
5	UNIVERSITAT DE VALENCIA	UVEG	Spain	M1	M36
6	STMICROELECTRONICS SRL	ST	Italy	M1	M36
7	UNIVERSITEIT GENT	UGent	Belgium	M1	M36

[1] **PU** = Public
PP = Restricted to other programme participants (including the Commission Services)
RE = Restricted to a group specified by the consortium (including the Commission Services)
CO = Confidential, only for members of the consortium (including the Commission Services)

Deliverable Responsible

Organization: imec
Contact Person: D. Van Thourhout
Address: imec
kapeldreef 75
3001, Heverlee
Belgium
Phone: +32 9 264 3438
E-mail: dries.vanthourhout@imec.be

Executive Summary

In this deliverable we report on the design, fabrication and characterisation of optical filters and electrostatically movable grating couplers. All devices are fabricated on the standard silicon photonics platform, with a 220nm silicon layer thickness.

We developed a library of optical filter designs for incorporation in the final system. These can be used to suppress noise coming from the system and in particular of a preamplifier. Devices with different characteristics were demonstrated and further developed:

- Standard AWG filters with Gaussian response (BW ~ 1.7nm)
- MMI-AWG devices with flat passband response (BW ~ 3.3nm)
- Single ring filters with sharp Lorentzian response (BW ~ 0.34nm)
- Double ring filters with flat passband response and high crosstalk rejection (BW ~ 1.12nm)

The actual filter to be included in the final system will be determined based on system simulations in WP6.

In the work on the electrostatically movable grating couplers we focus on in-plane movable devices. We developed the underetching processes needed to create large scale freehanging structures. Using these we demonstrated lateral movement of the grating couplers, over a distance of at least 0.7μm. This is sufficient to compensate for typical misalignment errors in the fiber-chip coupling process and with further development could help in reducing the cost of fiber-chip packaging.

Change Records

Version	Date	Changes	Author
0.1 (draft)	2014-01-10	Start	Dries Van Thourhout
1.0 (submission)	2014-02-12	Update table of content	Dries Van Thourhout

1 *Contents*

2 Introduction

This deliverable reports on the design, fabrication and testing of the WP5 optical filters and first generation beam shapers. This report follows milestones MS27 (design) and MS31 (fabrication) and is extended with measurement results on the related devices.

The targeted specifications for these components were respectively:

- **Optical filter**: 2/3nm bandwidth[2], >10dB suppression, >30nm FSR
- **Coupler**: design and evaluate an electro-mechanically controllable grating coupler

3 Optical filter

3.1 Introduction

Optical filters are used in various ways in optical networks. In WDM-networks (Wavelength division multiplexing) they can be used for multiplexing/demultiplexing optical signals or dropping/adding single signals in add-drop nodes. NAVOLCHI is focussing on single wavelength links and in that case the filter might be relevant for suppressing unwanted noise before the detector, certainly if a pre-amplifier is used (see WP4). The specifications set forward in the proposal for this filter were:

- **Optical filter**: 2/3nm bandwidth[3], >10dB suppression, >30nm FSR

It was assumed that the system study carried out in NAVOLCHI would further refine these specifications but at the time of the design of these filters no further specifications were available. Therefore we focused on two large classes of filters, AWG-based and ring resonator based and evaluated/improved their performance. Based on these we discuss the different design trade-offs. If a filter is required in the final demonstrator, it can be selected based on the results described here.

3.2 Fabrication

All devices were fabricated on 200mm wafers using imec's standard passive waveguide platform, starting from SOI-wafers (SOITEC) with a 220nm thick silicon layer. Patterns were defined using 193nm DUV lithography and subsequently etched using a dry etching process (ICP-based). Two etching steps were used:

- A 220 nm deep etch to define the fully etched waveguides

[2] Note there is an inconsistency in the DoW regarding the specifications of the bandwidth for the filter. The MS27 mentioned 3nm while the resulting deliverable mentions 2nm. We have now designed devices with different bandwidth, demonstrating our design approaches are flexible with respect to the bandwidth. The bandwidth for the final design will be selected on the basis of the system specifications.

[3] Note there is an inconsistency in the DoW regarding the specifications of the bandwidth for the filter. The MS27 mentioned 3nm while the resulting deliverable mentions 2nm. We have now designed devices with different bandwidth, demonstrating our design approaches are flexible with respect to the bandwidth. The bandwidth for the final design will be selected on the basis of the system specifications.

- A 70 nm shallow etch to define grating couplers and transition regions between deeply etched regions and slab regions.

Following fabrication wafers were diced for characterisation.

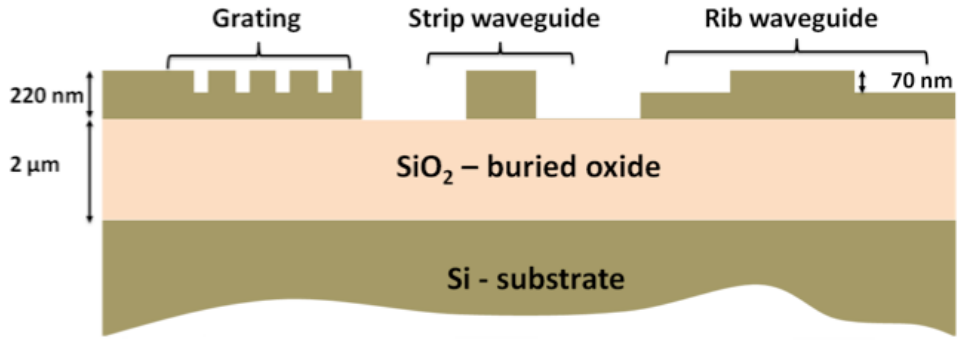

Figure 1 The different photonic components fabricated in IMEC on the SOI structure; the deep etch of 220 nm is used in fabricating the strip wave- guides whereas the shallow etch of 70 nm is used in making the rib waveguides and the gratings.

In some cases the filters were further processed and heaters were added for tuning the resonance frequency.

3.3 AWG-based filters

AWG (arrayed waveguide grating router) filters are very popular integrated photonics filters for multiplexing and demultiplexing optical wavelength channels. They have been fabricated in many different material systems, including silicon-on-insulator (SOI). When fabricated in silicon they suffer from somewhat higher crosstalk[4] then when fabricated in lower index contrast systems but through optimizing the design we managed to routinely reach better than 20dB and even 25dB for devices with up to 16-channels and with down to 200 GHz channel spacing [1]. Given their nice filter response, AWG-devices can also be used as stand-alone filters, e.g. for suppressing unwanted noise at frequencies away from the main wavelength channel. Standard AWG-based filters have a Guassian-like passband. In some cases this might be sufficient but in some cases a broader and more box-like transfer is desired. Therefore we investigated in more detail the option of including an MMI (multi-mode interference coupler) at the entrance of the first star coupler of an AWG demultiplexer, as schematically shown in Figure 2a). This MMI widens the field at the input. As a consequence also the field imaged at the exit of the output star coupler is widened, which, after convolution with the field of the output waveguide results in a broadening of the optical response. This approach was successfully demonstrated in other material systems by other groups and by us in SOI in an earlier project (WADIMOS). Here we evaluated this approach in more detail, investigating the influence of more parameters. Figure 2b shows the simulated field profile in the MMI, for different widths of this MMI.

[4] Due to phase noise accumulated in the dispersive waveguide array

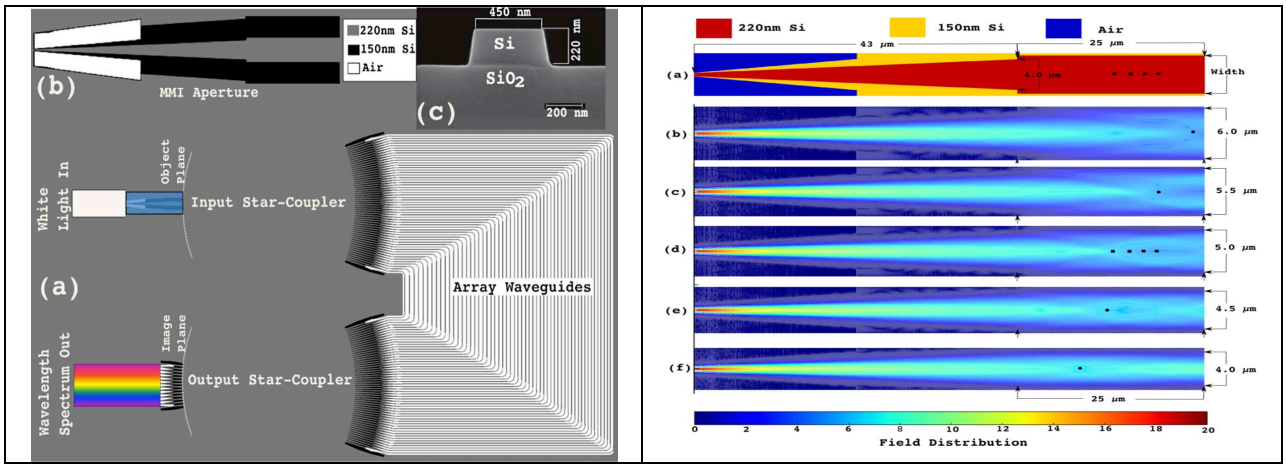

Figure 2 a) Global layout of flat-passband AWG with MMI-incoupler. b) Schematic and simulation of MMI based entrance section for AWG. Dots indicate optimal position for entrance of star coupler.

Figure 3a) shows a microscope picture of a fabricated MMI-AWG chip. The left part of the picture shows a global view, at the right insets show zoomed versions of the entrance of the star coupler (with a 15um long MMI) and of the array side of the star coupler. Figure 3b shows the calculated and measured response of MMI-AWGs with different MMI lengths. These figures show that the 15um long MMI exhibits the best compromise between improved passband width and losses. Therefore we focussed on these for the further characterisation.

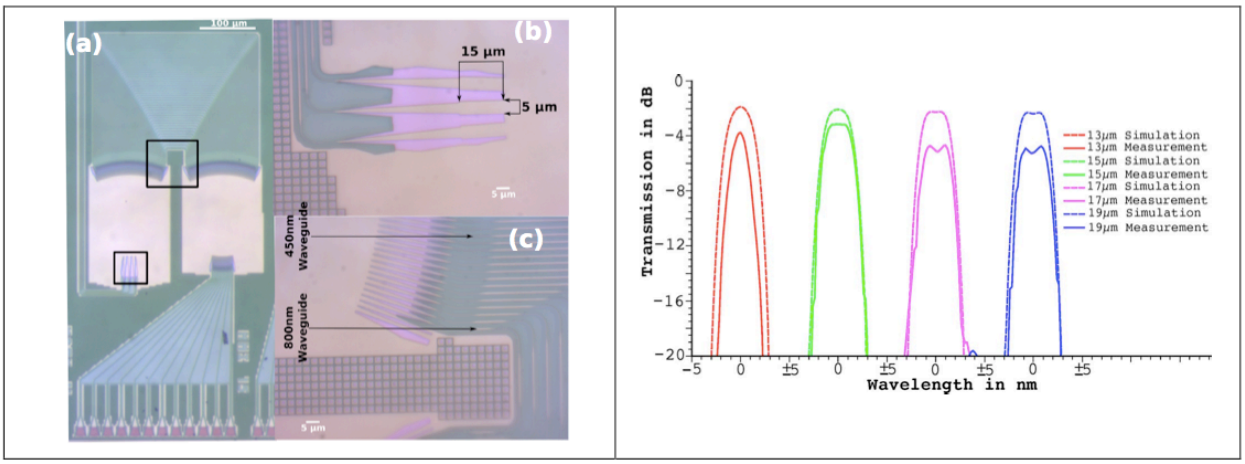

Figure 3 a) Microscope view of fabricated filter. b) Measured transmission for different MMI lengths

In Figure 4 we study the effect of the number of waveguide arms in the array of the AWG. The figure shows the simulated 1dB and 10dB bandwidths for both MMI-AWGs and standard AWGs. For the MMI-AWGs also the experimental results are shown. As expected the bandwidth decreases with increasing number of waveguides. It is obvious that the MMI-AWG shows a considerably larger bandwidth. Also the "aspect-ratio" is improved.

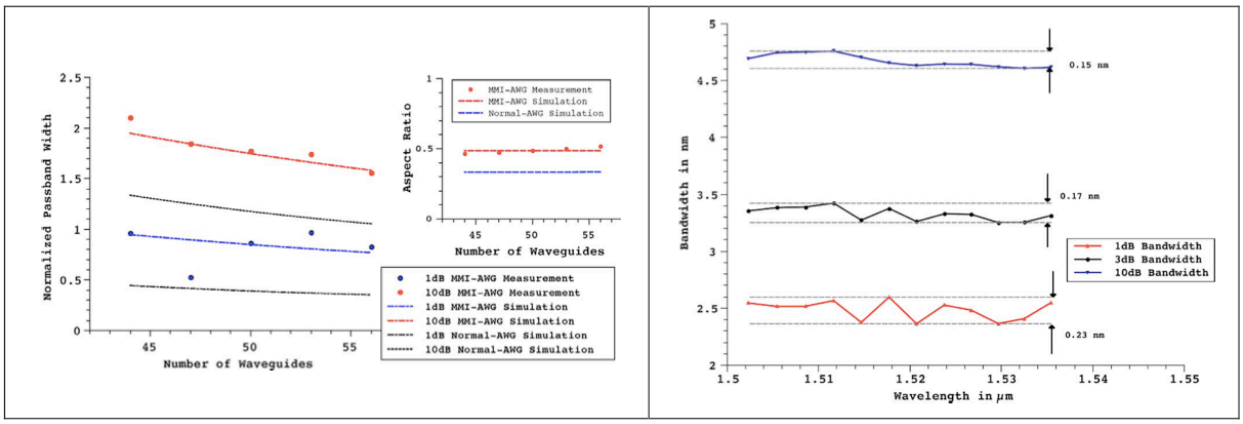

Figure 4 a) Passband width (passband width is normalized to the 400GHz channel spacing) vs. number of waveguides used in the waveguide array of the MMI-AWG. Inset shows the comparison of the aspect ratio between conventional-AWG and MMI-AWG. b) 1 dB, 3 dB and 10 dB bandwidth for 12×400 GHz MMI-AWG. Associated non-uniformity is indicated in the graph.

Figure 4b shows that the bandwidth is fairly constant as function of wavelength.

3.4 Ring based filters

Next to the AWG-based filters we also designed ring resonator based devices. We considered both single ring and double ring based configurations. Single ring resonators give a sharp response, which might be relevant if a narrow bandwidth signal needs to be filters. Higher order filters result in a larger bandwidth, with higher crosstalk suppression. Figure 5 shows a typicial mask layout for a ring based filter, designed here as a four channel device. The resonators are designed as racetracks and the length of the straight coupling sections, together with the gap in between is optimized to obtain the desired coupling strength between the bus and ring and ring/ring. The devices are equipped with heaters to tune the resonant wavelength to the desired position.

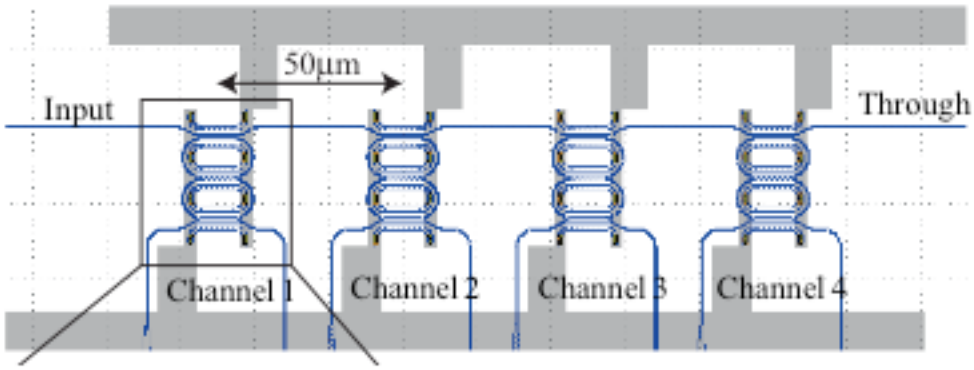

Figure 5 Mask layout of four channel double ring resonator filter.

An example of the response for a single ring resonator and a double ring resonator is given in Figure 6. The resonance wavelength can be tuned over a full period, over more then 10nm.

Compared to the AWG filters demonstrated earlier the ring resonators show a sharper filter response (0.34nm and 1.12nm for single and double ring devices respectively) and better crosstalk suppression (>20dB).

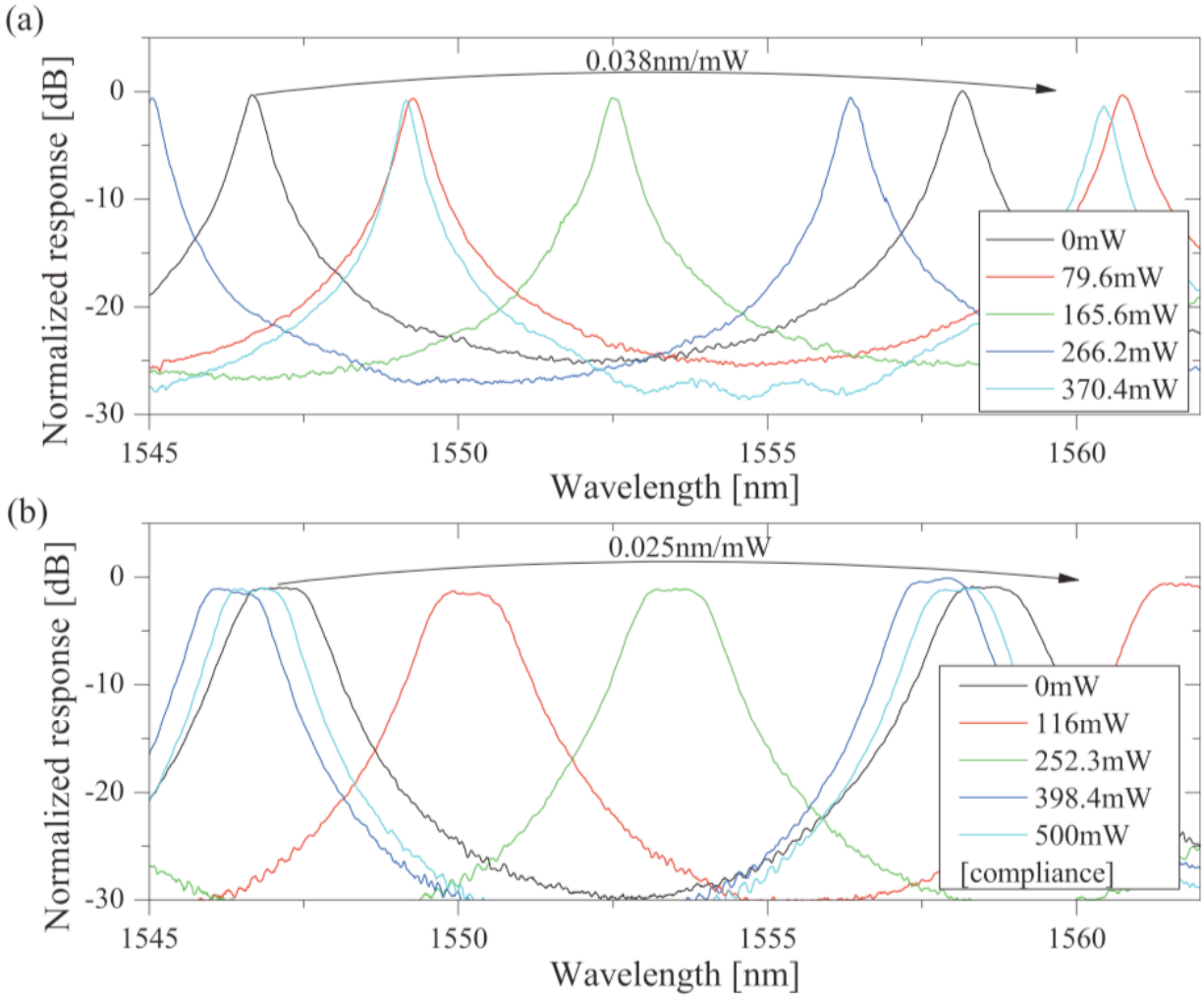

Figure 6 Filter response for single and double ring resonators, including heaters for shifting wavelength to desired position.

4 Optical coupler

4.1 Introduction

The original aim of this task was to design a focussing grating coupler, showing 5dB loss and 100um coupling distance. However, at the start of the project we decided to evaluate a completely new type grating couplers, which are electrostatically steerable. Several variations where designed:

1) Grating couplers steerable in plane, driven through comb actuators (Figure 7a).
2) Grating couplers steerable in angle, driven through parallel plate actuation (Figure 7b).

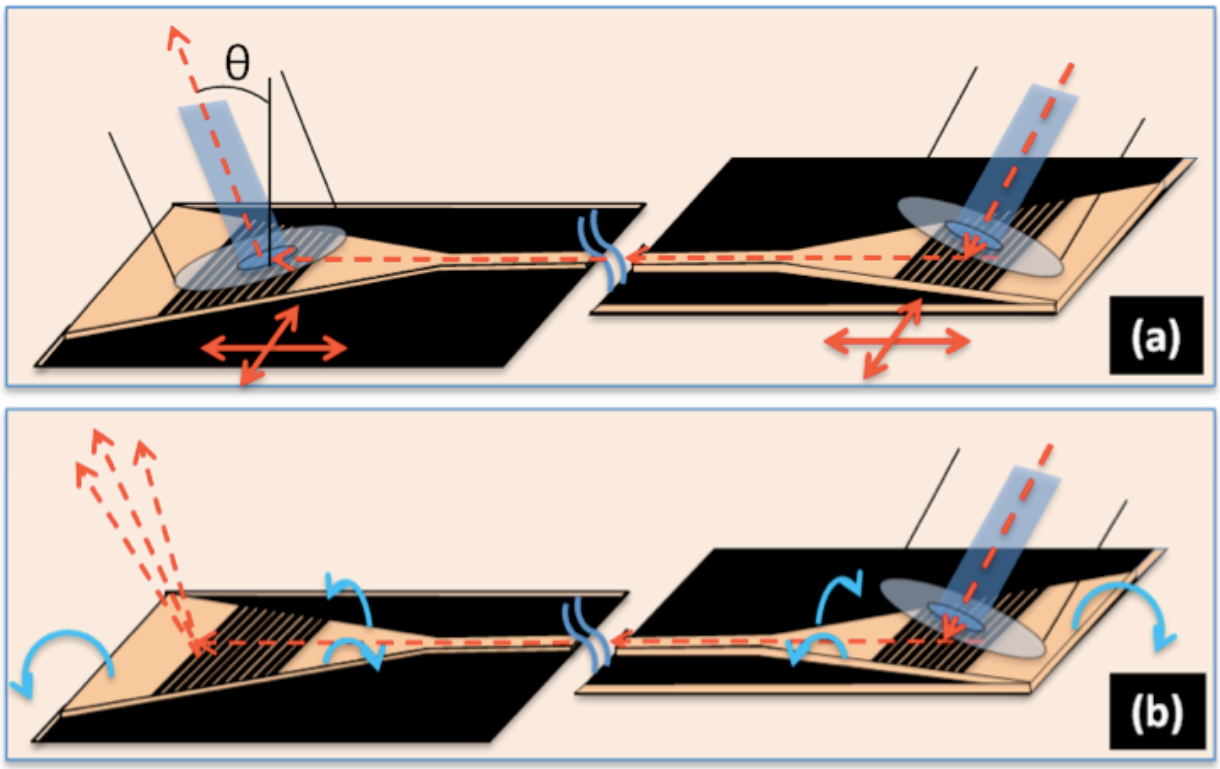

Figure 7 a) In plane movable grating couplers. b) Grating couplers steerable in angle.
Several variations for each of these have been implemented in a mask and have been fabricated. The in-plane steerable grating couplers were most successful and we will focus on those in the remainder of this deliverable.

4.2 Fabrication

The optical beam shapers were fabricated using the same process as the one used for the optical filters. However, since the optical beam shapers need to be free hanging, such that they can be moved electrostatically an underetching process had to be developed, to remove the oxide below the moving parts of the beam shapers. Typically a wet etch process would be used for that.
However, removal of the water from the liquid etchant results in a meniscus (liquid-air interface) that often pulls movable structures into contact via capillary forces. Once in contact, even after drying, the surfaces often remain in contact due to various types of adhesion forces (e.g. capillary, van Der Waals, electrostatic due to trapped charge) resulting in a stuck, or stiction-like failure as shown in Figure 8.

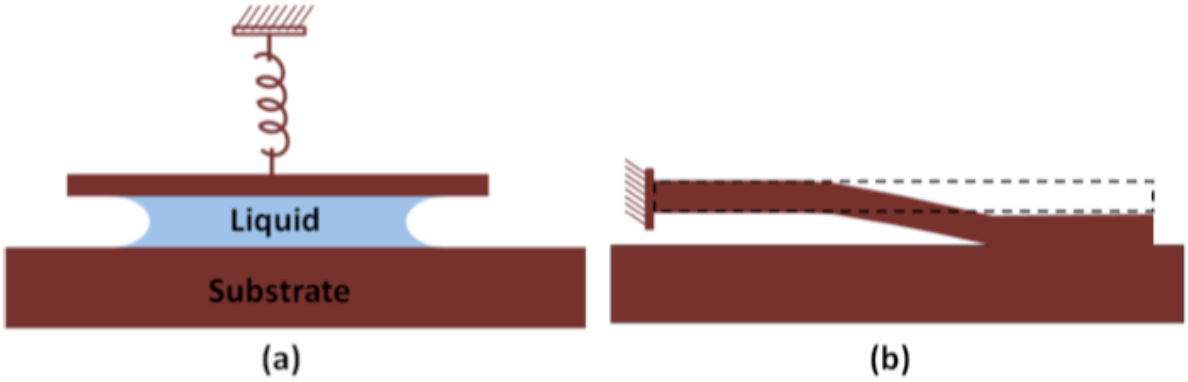

Figure 8 Schematic illustration of: (a) the formation of a liquid meniscus during the sacrifical etch, and (b) sticking of the released parts due to surface tension at the final phase of evaporation.

There are several solutions that have been used by researchers and MEMS manufacturers to reduce stiction. One approach calls for coating the substrate surface with a thin hydrophobic layer, thereby repelling liquid from the surface. Another popular technique is to dry surfaces using super-critical CO_2. This removes fluid without allowing the surface tension to form. Still other techniques utilize "stand-off bumps" on the underside of moving parts. These bumps act as pillars, propping up movable parts wherever surface tension may form. However, the most effective method for avoiding stiction is simply to use dry or quasi-dry etching techniques for release wherever possible.

A possible approach is to use a hydro-fluoric acid (HF) vapor phase etching (VPE) system. This enables the removal of silicon dioxide in a vaporous environment rather than in an aqueous solution. The silicon oxide is etched in a quasi-dry method and is never in contact with a liquid. No cleaning or rinsing of the chips is needed.

In this process water acts as initiator of the etching process as well as reactant. This fact suggests that the etching process can be temperature controlled to maintain the amount of water needed to initiate the process and the amount of reactant water in equilibrium.

We used the HF VPE apparatus from IDONUS to release all our MEMS devices. A detailed descriptipon of the working principle of the apparatus and its mechanical realisation can be found on www.idonus.com. In this system, the HF evaporates at room temperature and the etching process starts spontaneously. The etch rate is controlled by the wafer temperature that can be adjusted from 35°C to 60°C. The water film on the wafer is evaporated at moderate temperatures. We experimentally found that the etch rate decreases with increasing temperature and stops completely at temperatures above 52°C when using 50% concentrated HF.

Process optimization: Starting with a clean and dry surface of the samples was the most important pre-condition to obtain a uniform etching rate for successful release of the structural layers. Hence, the separate dies were first cleaned with acetone, IPA and de-ionized water and later dried with N_2. Next, the samples were thoroughly dried at an elevated temperature of 150C for 15 minutes to ensure that no moisture is left on the samples before they were put inside the VPE. Particularly, the metal deposited samples suffered from frequent stiction even after thorough cleaning and drying of the samples before starting the etching process. The situation worsened with any residual resist left on the samples after the lift-off. Additionally, after a long etching time (~ 2-2.5 hrs), we observed peeling of the metal layers deposited on top of the Si structure. Hence, we had to add an intermediate step of rapid thermal annealing of the metal deposited samples at 430°C to enhance the adhesion of the Au films deposited on Si. Even after

taking all the precautions, we observed non uniform etching and sticking of the released samples when etched at temperatures lower than 40 ◦C.
However, we could achieve a stiction free release of our devices when the buried oxide was etched at a temperature of ≥42◦C which resulted in a etch rate of ~ 5-6 μm/ hr. In this way, we could obtain a reproducible etching process though a few inconsistencies remained.
Figure 9 shows an example where 220 nm thick and 2 μm wide Si cantilevers with length upto 200 μm are released successfully without stiction after removing the 2 μm thick SiO_2 layer. For these devices, we had to go to higher temperature of 43.5C to release the longer cantilevers, which gave us an etching rate of ~1 μm/ hr.

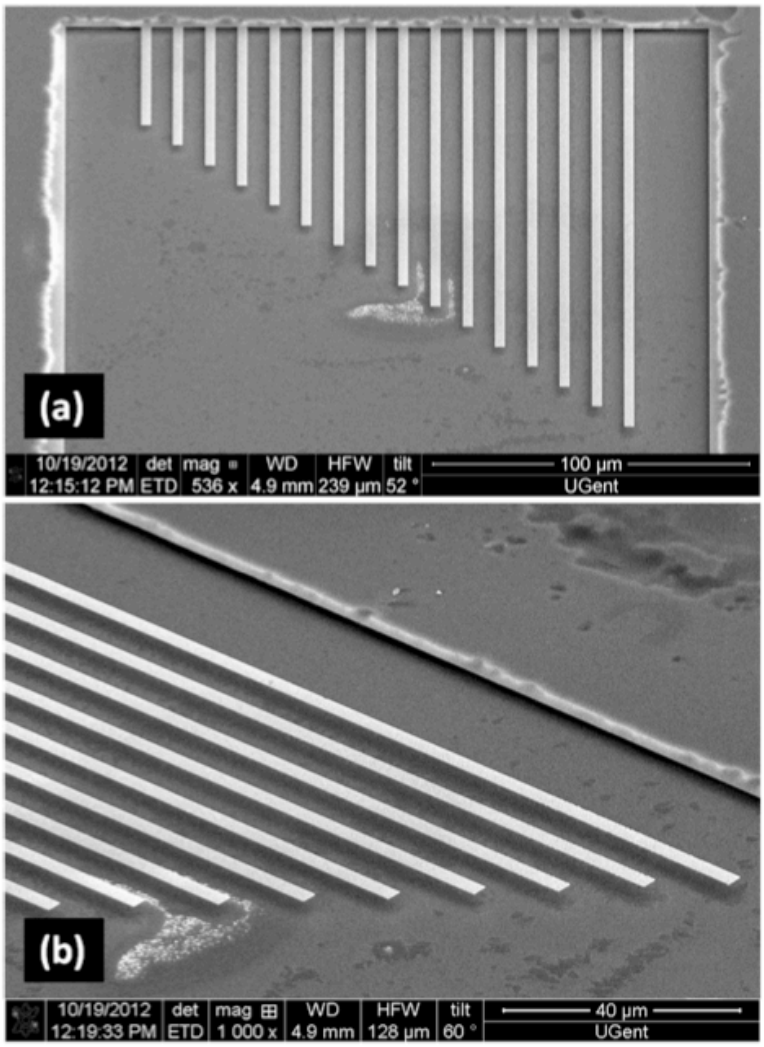

Figure 9 SEM pictures of the successful release of 220 nm thick and 2 μm wide poly-Si cantilevers on top of 2 μm thick SiO_2 without sticking; where the length of the cantilevers varies from 50 μm to 200 μm.

4.3 Design of the in-plane moving grating coupler

SEM pictures of the in plane moving device are given in Figure 10. The actuator consists of 3 major elements:

1. The first is the focused grating coupler (FGC) which is the principal micro-optical component of the device and the central component of the active region. To decrease the weight of the proof mass (here the FGC) attached to the comb drives, the FGC is cut down from the sides and the top, making it smaller and lighter
2. The second is a system of curved compliant suspension beams. The curved 'S' shape is designed to convert a unidirectional actuation into a bidirectional displacement
3. The third element comprises of comb-drive actuators where the moving fingers are attached to a rigid frame which is further attached to the fixed parts of the chip by 'V' shaped springs.

The active FGC along with the movable comb fingers (region A) are always kept at ground potential whereas the two separate fixed comb structures (region B and C) are always maintained either at ground or higher potential respectively depending on the direction of the desired movement. These three regions A, B and C are etched completely through the silicon, allowing for separate electrical actuation.
In our design each of the comb drive actuator consists of 28 pairs of fingers of 300 nm width, 2 μm length and 300 nm gap between each pair. The rigid support is 1.5 μm wide and 56 μm long. The 'V' shaped springs are 120 nm wide and 18 μm long and are connected by another 0.75 μm wide rigid structure. The 'S' shaped connectors are 29 μm long and 0.75 μm wide.

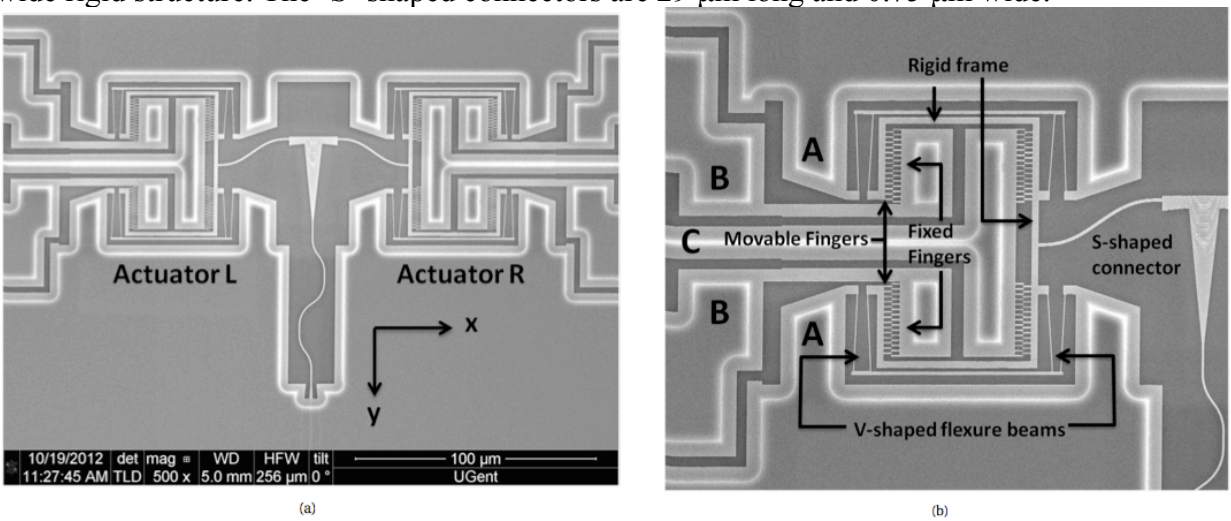

Figure 10 (a) SEM picture of the top view of the planar moving devices showing the two actuators on both the sides of the FGC (a), and close-up view of the specific actuators and the different components of it (b).
The comb drives were optimised using finite element simulations as shown in Figure 11. A comb-drive typically can only apply a force in a single direction. Moving along the x-axis is trivial: one only has to actuate a single comb (Figure 11a). By actuating both combs simultaneously however, and optimizing the shape of the S-like beams holding the grating couplers in principle also movement along the waveguide axis (y-direction) should be possible as shown in the simulation of Figure 11b. By doubling the combs as shown in the fabricated devices (Figure 10), further flexibility is introduced.

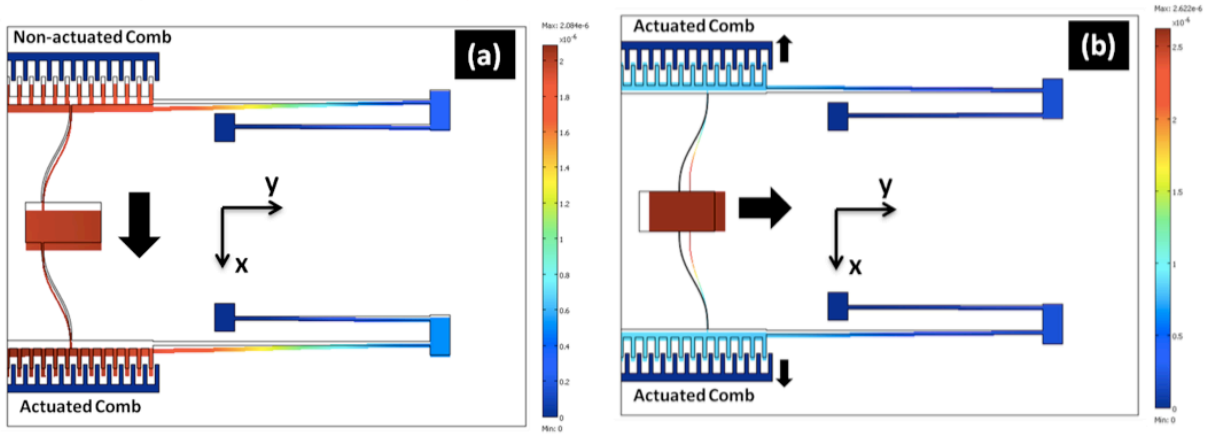

Figure 11 a) Moving along x-axis through actuation of single comb-drive. b) Moving along y-axis through actuation of both comb-drives simultaneously.

4.4 Measurement results

We relied our measurements on the deviation of the optimum alignment between the grating coupler and the single mode fiber (SMF). Hence, in the non-actuated condition of the device, the fiber is aligned such that the transmission between the FGC and the fiber is maximized. Then, the two different actuators 'R' and 'L' are actuated together or separately to achieve the displacement of the FGC in the desired direction.

Figure 12 shows one such example where the FGC is actuated in the negative x direction. For this, when the pads 'A' and 'B' (Figure 10) were kept at the ground potential, pad 'C' was at a higher potential for actuator L which actuates the connected comb drives. Similarly, for the actuator R, the disconnected combs were actuated which helps together with actuator L in pushing the FGC towards the negative X direction. The transmission spectra are shown in Figure 12a for the different positions of the FGC and the SMF. For clarity, we performed a 3rd order polynomial fit of each spectrum as shown in Figure 12b. As can be observed, at an applied voltage of ~ 22 V, an additional loss of 0.4 dB was measured. To confirm the direction of movement of the FGC, we then shifted the fiber in the negative X direction and we could successfully reach back to the initial intensity at the same central wavelength of the FGC. Further, as we again go back to the non-actuated state as before keeping the SMF position fixed, the intensity again drops down because of the mismatch between the SMF and the FGC. Once, we move the SMF in the opposite direction from the previous one, the optimum alignment is achieved again.

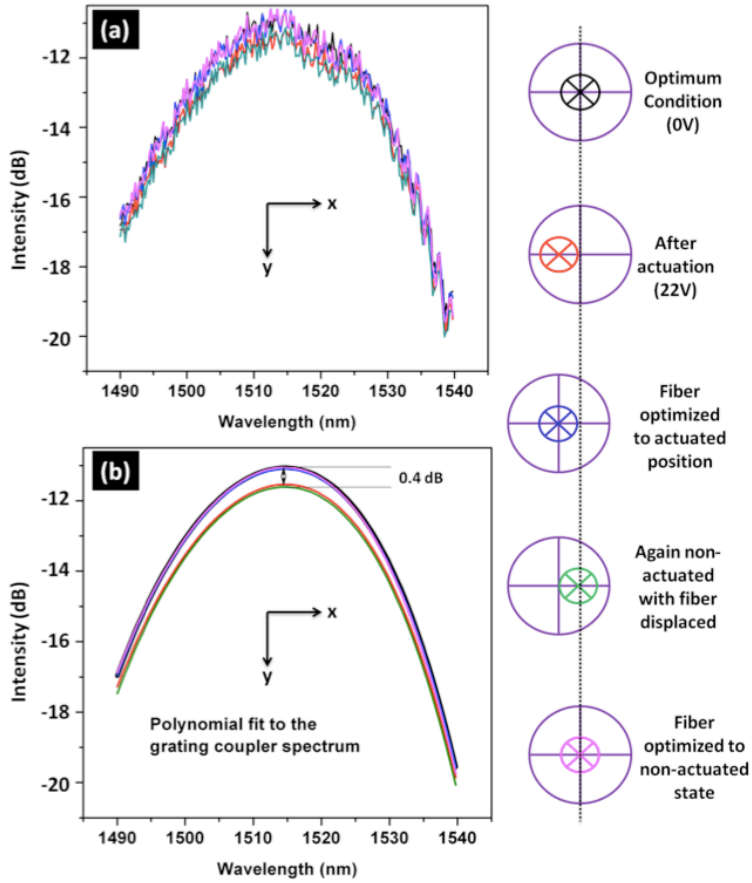

Figure 12 Change in transmission spectra of the grating coupler (a) when the FGC is displaced along the negative x-direction due to actuation of the comb drives, (b) 3rd order polynomial fit of the transmission spectra clearly indicating the change in intensity level with the displacement of the FGC (The big circle represented the SMF whereas the smaller crossed circle represents the FGC).

Figure 13 shows another approach to prove the movement of the FGC in the positive X direction. Here, we first moved the SMF in the positive X direction to intentionally introduce an aligment loss of 0.3 dB. Thereafter, the actuator R and L are moved together to push the FGC to the right and as can be observed, we could again reach the same intensity distribution as in the non-actuated condition (Figure 13a). Later, we moved the SMF in the negative X direction from the optimum alignment condition and as we further push the FGC rightwards, due to an increased misalignment, the intensity at the central wavelength drops down further as can be observed from Figure 13b.

Hence, Figure 12 and Figure 13 together shows the successful implementation of the lateral movement of the FGC through the synchronized movement of the actuator 'L' and 'R' in the same direction.

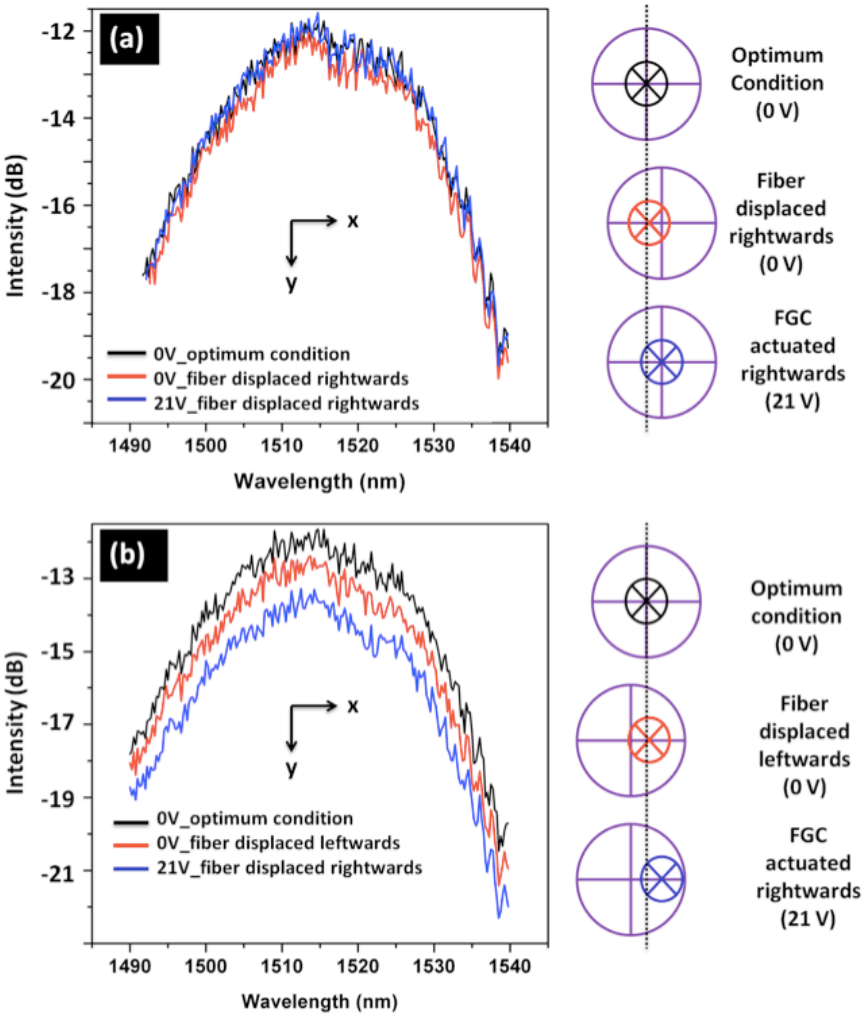

Figure 13 Change in transmission spectra of the grating coupler when the FGC is displaced along the positive x-direction with the fiber displaced in the same direction (a) and in the opposite direction (b) (The big circle represented the SMF whereas the smaller crossed circle represents the FGC).

However, when trying to actuate both comb drives together, no clear results were obtained. As mentioned earlier, when the two actuators move in the opposite directions, the 'S' shaped flexures either should get stretched or compressed making the FGC to move in the positive or negative Y direction respectively. Though we are not fully sure of what could be the exact reason behind the non-performance of the stretching and compressing of the 'S' beams in the desired manner, one reason could be the deeply etched single mode waveguide which connects the FGC and the passive region. We designed the spring shape of the waveguide so that it gets compressed and extended following the movement of the FGC in the ± Y direction. But, unlike deforming a long spring side- wise, more force is needed to shorten or elongate them. Hence, it might be that the force imposed on the waveguide by the FGC is not large enough to deform it along its length.

Another possible reason of the failure of the mechanism could be the width of the designed 'S' beams which we kept to be 0.75 µm. With larger width, stretching or compressing the 'S' beams becomes more and more difficult which in-turn deteriorates the whole mechanism. Hence, to our understanding, though the lateral displacement (X direction) of the FGC works perfectly, these

two reasons individually or together might have influenced the non-performance of the mechanism in the (Y) direction.

5 Conclusion

In this deliverable we reported on the design, fabrication and characterisation of optical filters and electrostatically movable grating couplers. Through the work on the optical filters we now have a library of possible filter designs for incorporation in the final system:

- Standard AWG filters with Gaussian response (BW ~ 1.7nm)
- MMI-AWG devices with flat passband response (BW ~ 3.3nm)
- Single ring filters with sharp Lorentzian response (BW ~ 0.34nm)
- Double ring filters with flat passband response and high crosstalk rejection (BW ~ 1.12nm)

The actual filter to be included in the final system will be determined based on system simulations in WP6.

In the work on the electrostatically movable grating couplers we focussed on in-plane movable devices. We developed the underetching processes needed to create large scale freehanging structures. Using these we demonstrated lateral movement of the grating couplers, over a distance of at least 0.7μm. This is sufficient to compensate for typical misalignment errors in the fiber-chip coupling process and with further development could help in reducing the cost of fiber-chip packaging.

6 References

[1] S. Pathak, D. Van Thourhout, and W. Bogaerts, “Design trade-offs for silicon-on-insulator-based AWGs for (de)multiplexer applications.,” *Opt. Lett.*, vol. 38, no. 16, pp. 2961–4, Aug. 2013.